Doppler spectra of airborne sound backscattered by the free surface of a shallow turbulent water flow

Giulio Dolcetti, Anton Krynkin, and Kirill V. Horoshenkov

Articles you may be interested in

Doppler spectra of airborne sound backscattered by the free surface of a shallow turbulent water flow

Giulio Dolcetti,[a] Anton Krynkin, and Kirill V. Horoshenkov

Department of Mechanical Engineering, The University of Sheffield, Mappin Street, S1 3JD, Sheffield, United Kingdom

Measurements of the Doppler spectra of airborne ultrasound backscattered by the rough dynamic surface of a shallow turbulent flow are presented in this paper. The interpretation of the observed acoustic signal behavior is provided by means of a Monte Carlo simulation based on the Kirchhoff approximation and on a linear random-phase model of the water surface elevation. Results suggest that the main scattering mechanism is from capillary waves with small amplitude. Waves that travel at the same velocity of the flow, as well as dispersive waves that travel at a range of velocities, are detected, studied, and used in the acoustic Doppler analysis. The dispersive surface waves are not observed when the flow velocity is slow compared to their characteristic velocity. Relatively wide peaks in the experimental spectra also suggest the existence of nonlinear modulations of the short capillary waves, or their propagation in a wide range of directions. The variability of the Doppler spectra with the conditions of the flow can affect the accuracy of the flow velocity estimations based on backscattering Doppler. A set of different methods to estimate this velocity accurately and remotely at different ranges of flow conditions is suggested. © *2017 Author(s). All article content, except where otherwise noted, is licensed under a Creative Commons Attribution (CC BY) license (http://creativecommons.org/licenses/by/4.0/).* https://doi.org/10.1121/1.5015990

I. INTRODUCTION

The ability to measure the velocity of sea currents from the Doppler spectra of airborne waves backscattered by the water surface has been well established in the past. Although these measurements can be obtained in principle using acoustic waves,[1] most applications have been based on radio waves[2] or microwave[3,4] historically. These measurements are typically performed within the so-called Fraunhofer zone, where the size of the scattering region of the rough surface is small compared to the distance from the source and receiver. In this condition, the dominant Bragg scattering mechanism produces peaks of the first-order Doppler spectrum[5] at the frequencies of the surface waves with the wavelength of approximately half the incident wavelength. The flow velocity near the surface can be estimated based on the frequency shift of the Bragg peaks caused by the advection due to the current.[2]

The same technique has been applied in order to estimate the surface velocity of rivers, in a few studies.[6,7] Lower costs, safer access, and less likelihood of damage from floating debris make non-contact flow velocity sensors based on airborne Doppler an attractive alternative to intrusive flow velocity measurement, but the interpretation of the data is not as straightforward as it is in the ocean,[6] and the accuracy of the measurements varies greatly at different flow conditions.[8] This is attributed to a relatively poor understanding of the dynamic behavior of the water surface in rivers and open channel flows compared to that in the ocean.

The scattering of airborne or underwater acoustic waves by the water surface is described by similar physical principles to the scattering of electromagnetic waves, although it is not sensitive to polarization. The Doppler spectra of underwater sound scattered by wind-waves are related to those of airborne microwave.[9] When acoustic waves are scattered on the air side, the water surface can be considered as rigid, which simplifies the scattering problem considerably. On the other hand, ultrasound dissipates relatively rapidly with distance from the source, and ultrasonic transducers often have a wider directivity in air compared to microwave or radar sources. Because of the wider directivity of the transducer, the measurements are often performed outside of the Fraunhofer zone, where the typical interpretation of the Doppler spectra based on Bragg scattering has no rigorous justification. The only known scientific study so far that dealt with the Doppler spectra of airborne ultrasound in rivers[10] was a field work, with no examples of the measured Doppler spectra. An analysis of the scattering phenomenon in realistic conditions, accompanied by a simultaneous characterization of the water surface statistics, is required in order to establish the potential of rigorous non-contact flow monitoring techniques based on ultrasound.

This work presents the Doppler spectra of airborne ultrasound backscattered by the water surface of a wide range of flows, measured in a laboratory flume. A recent study[11] has shown that the characteristic spatial and temporal scales of the instantaneous water surface elevation in the same range of flow conditions used for this study are related to the main hydraulic quantities (namely, the mean flow depth and the mean surface velocity). Based on this

[a] Electronic mail: g.dolcetti@sheffield.ac.uk

improved understanding of the surface dynamics, a linear random phase model of the water surface was developed. The Doppler spectra were predicted by a numerical Monte Carlo simulation based on the Kirchhoff approximation. The comparison aimed at providing a rigorous interpretation of the measured spectra, in order to improve the accuracy and reliability of the flow velocity estimations with airborne acoustic sensors. A set of analysis techniques that enable this estimation is presented, and the applicability of each technique at different flow conditions is discussed by means of a comparison with the experimental data.

The paper is organized in the following manner. The experimental acoustic setup and the hydraulic conditions of the investigated flows are reported in Sec. II. The numerical model is described in Sec. III. Experimental and numerical results are presented in Sec. IV. The principal implications for the remote measurement of the flow velocity based on backscattering Doppler are presented in Sec. V. Section VI summarizes the main results of the study.

II. EXPERIMENTAL SETUP

A. Acoustic setup

Ultrasound with the frequency of 43 kHz was generated above the water surface with a 70 mm directional ultrasonic transducer (Pro-Wave ceramic type 043SR750) and recorded with a 1/4 in. Brüel & Kjær (B&K) 4939-A-011 microphone with type 2670 pre-amplifier. The transducer and the microphone were installed in a 12.6 m long and 0.459 m wide rectangular laboratory flume, at the distance of 8 m from the flume inlet and 0.2295 m from the flume side walls, along the flume centerline. A schematic of the acoustic setup is shown in Fig. 1. The transducer and the microphone were facing in the direction of the inlet, with their axis inclined downwards by the same angle $\psi_1 = \psi_2$ equal to 30° with respect to a plane parallel to the flume bed. Water was circulated in the flume below them. The height of the microphone and of the transducer with respect to the flume bed was adjusted every time the flow condition was changed, thus ensuring that the height of the source with respect to the average height of the water surface, z_1, was approximately 200 mm. Due to the dynamic fluctuation of the water surface, the uncertainty of this measure was estimated to be of the same magnitude as the standard deviation of the surface elevation, σ, which varied between 0.05 and 2.03 mm across the different flow conditions (see Table I).

The maximum amplitude of the incident acoustic field was found along the axis of the transducer, where the directivity had a maximum. A system of co-ordinates was defined with the center located at the intersection between the axis of the transducer and the ideal plane that cuts through the mean elevation of the rough water surface. The x axis was along the flume centerline, parallel to the mean flow direction, and the z-axis was perpendicular to the plane of the mean surface, pointing upwards. In this system of co-ordinates, the co-ordinate vectors of the transducer and of the microphone in millimeters were $\mathbf{S} = (346.4, 0, 200.0)$ and $\mathbf{M} = (376.1, 0, 152.6)$, respectively.
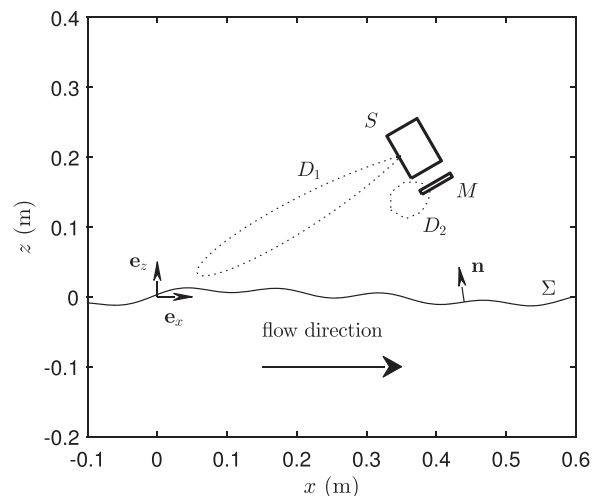

FIG. 1. A schematic of the measurement setup. The acoustic transducer indicated by the letter S emitted ultrasound with the directivity pattern D_1. This was scattered by the rough surface Σ with normal $\mathbf{n}$, and recorded by a microphone M with the angular response function D_2.

The acoustic pressure field generated by the ultrasonic transducer at the distance R from its center and at the angle θ_1 from its axis can be approximated in the far-field (where $\kappa R \gg 1$, and κ is the acoustic wavenumber) as[15]

$$P(R, \theta_1) = D_1(\theta_1)G_0(R), \qquad (1)$$

where G_0 is the free-field Green's function and D_1 is the complex-valued directivity pattern of the transducer.

The directivity pattern of the ceramic transducer used for the experiments was measured in an anechoic chamber at the frequency of 43 kHz. In order to measure the directivity, the transducer was mounted horizontally on top of an automated rotating table, and the amplitude and phase of the acoustic field were measured at different instants while the table performed a 360° revolution, with the angular resolution of 0.04°. The directivity was measured at the distances

TABLE I. Test flow conditions. The Froude number, $U_0/\sqrt{gH}$, increases from condition 1 to 13, where U_0 is the flow mean surface velocity, H is the flow mean depth, and g is the gravity constant. Re is the flow Reynolds number, $U_0 H/\nu$, where ν is the kinematic viscosity of water. σ and k_0 correspond to the characteristic amplitude and the characteristic wavenumber of the surface elevation, respectively.

Flow cond.	H (mm)	U_0 (m/s)	F	Re	σ (mm)	k_0 (rad/m)
1	42.2	0.19	0.30	8.0×10^3	0.05	—
2	72.9	0.35	0.41	2.5×10^4	0.40	84.3
3	101.0	0.41	0.41	4.1×10^4	0.50	59.9
4	42.2	0.30	0.47	1.3×10^4	0.25	120.8
5	101.3	0.49	0.49	4.9×10^4	1.79	41.4
6	43.0	0.34	0.52	1.5×10^4	0.49	89.9
7	73.1	0.46	0.54	3.4×10^4	1.21	47.0
8	40.5	0.36	0.57	1.5×10^4	0.34	78.9
9	43.4	0.40	0.61	1.7×10^4	0.46	62.5
10	99.0	0.60	0.61	5.9×10^4	2.03	27.1
11	72.4	0.54	0.64	3.7×10^4	1.17	33.4
12	43.1	0.43	0.66	1.8×10^4	0.57	53.1
13	73.2	0.58	0.68	4.2×10^4	1.10	28.4

3388   J. Acoust. Soc. Am. **142** (6), December 2017

Dolcetti *et al.*

of 200 and 400 mm from the center of the source and these measurements differed by 12% at most. The two measurements were then averaged in order to define an equivalent directivity. The average directivity displayed small random fluctuations with the amplitude smaller than 2.5% of the maximum of the absolute directivity, which were attributed to the measurement uncertainty. These small fluctuations caused larger uncertainties in the calculation of the derivative of the directivity with respect to the angle, which was required for the calculation of the acoustic field scattered by a rough rigid surface based on the Kirchhoff approximation. A moving average with a window of 4° was therefore applied to the averaged directivity in order to reduce the effects of these fluctuations.

By analogy with the definition of the directivity pattern of the transducer, the angular response of the microphone was represented by a function $D_2(\theta_2)$, where θ_2 was the angle with respect to the axis of the microphone. The B&K microphone used for the experiments had a broad angular response function D_2, which was determined at the frequency of 43 kHz based on the factory documentation.

The characteristic size of the insonified area was estimated as the region where the absolute value of the projected source directivity was at least half of its maximum. This area had the dimensions of 239 mm along the x-direction (parallel to the flow direction) and 56 mm along the y-direction (perpendicular to the flow direction), when the transducer was installed in the conditions shown in Fig. 1. The dimensions of the insonified area were comparable with the height z_1, therefore the variations of the geometric parameters and of the wavenumber vector of the incident acoustic wave across the whole rough surface had to be considered. Nevertheless, one can expect a relatively larger contribution coming from the region near the center of the insonified area, where the directivity had a maximum. Considering plane acoustic waves with the wavenumber κ incident upon the rough surface at the centre of this region, the reflected acoustic field is dominated by the interaction with the surface waves that satisfy the Bragg resonance condition.[5] These Bragg-resonant waves have the wavenumber

$$k_B = \kappa\left(\frac{x_1}{|\mathbf{S}|} + \frac{x_2}{|\mathbf{M}|}\right), \tag{2}$$

where x_1 and x_2 are the x-co-ordinates of the source and of the receiver, respectively. In this study, the acoustic wavelength was $2\pi/\kappa = 7.9$ mm, and the wavenumber of the Bragg-resonant waves calculated by Eq. (2) was equal to 4.4 mm, which is representative of capillary waves which dynamics are dominated by surface tension effects.

B. Water surface parameters

The experiments were performed at a range of subcritical flow conditions, each one characterized by different dynamic and geometrical parameters of the water surface. The flume bed in all measurements was covered with three layers of plastic spheres arranged according to a hexagonal compact lattice. Each sphere had the diameter of 25.4 mm.

The flume slope s and the flow discharge could be adjusted in order to obtain the desired combination of the mean water depth, H, and of the mean flow velocity at the surface, U_0. These parameters determine the characteristic spatial and temporal scales of the water surface,[11] which are represented by a characteristic surface wavenumber, k_0, and by a characteristic frequency, $k_0 U_0$. k_0 corresponds to the wavenumber of the stationary gravity waves that propagate against the flow with the phase velocity equal to U_0. Its value can be calculated by taking into account the vertical variation of the time-averaged streamwise velocity in the flow,[12,13] or more simply as the solution of [Ref. 12, Eq. (13)]

$$k_0 U_0 = \sqrt{\left(g + \frac{\gamma}{\rho}k_0^2\right)k_0 \tanh(k_0 H)}, \tag{3}$$

which can be obtained by approximating the time-averaged streamwise velocity at any depth with its value near the surface, U_0. In Eq. (3), g is the gravity constant, and γ and ρ are the water surface tension coefficient and density, respectively. In the range of flow conditions investigated here, the inclusion of the vertical streamwise velocity profile noticeably improves the accuracy of k_0 and of the dispersion relation only at relatively large Froude numbers,[11] $F = U_0/\sqrt{gH}$, and for long waves that do not play a dominant role for the acoustic backscattering. Therefore, in this work, the wavenumber k_0 was calculated based on Eq. (3), neglecting the vertical variation of the time-averaged flow velocity. With this assumption, the dispersion relation of gravity-capillary waves is expressed by

$$\Omega_w(k, \beta) = kU_0|\cos(\beta)|$$
$$+ \text{sign}(\cos(\beta))\sqrt{\left(g + \frac{\gamma}{\rho}k^2\right)k \tanh(kH)}, \tag{4}$$

where $\Omega_w(k, \beta)$ is the angular frequency of the surface fluctuations associated with a gravity-capillary wave with the wavenumber modulus k, and which propagates at the angle β with respect to the streamwise x-direction. Terms of the surface roughness which are not associated with gravity-capillary waves are not dispersive, and are advected rigidly at the velocity U_0 parallel to the x-direction. Their angular frequency $\Omega_U(k, \beta)$ is described by

$$\Omega_U(k, \beta) = kU_0|\cos(\beta)|. \tag{5}$$

A suitable measure of the variation of the surface elevation is represented by its standard deviation, σ. This was measured directly at multiple locations along the flume using arrays of conductance wave probes. Details of these measurements and of the hydraulic conditions have been reported in Ref. 11.

The characteristic parameters of the surface are reported for each flow condition in Table I, together with the Froude and Reynolds, $Re = U_0 H/\nu$, numbers based on the mean flow depth and mean surface velocity, where ν is the kinematic viscosity of water. The value of k_0 is not reported for flow condition 1, because this condition had the mean surface velocity smaller than the minimum phase velocity of gravity-capillary waves in still water, therefore stationary waves could not form.

J. Acoust. Soc. Am. **142** (6), December 2017

Dolcetti *et al.*   3389

III. NUMERICAL MODEL

A. Acoustic model

The Kirchhoff approximation can be used in order to describe scattering from a smooth surface, where the condition

$$\kappa R_c \sin^3 \psi \gg 1 \tag{6}$$

is satisfied. In Eq. (6), R_c is the curvature radius of the scattering surface, κ is the acoustic wavenumber, and ψ is the angle of incidence of the acoustic waves, determined by the inclination of the transducer and microphone (see Fig. 2). $\kappa R_c \sin^3 \psi$ is called the Kirchhoff parameter. According to the Kirchhoff approximation, the acoustic potential field generated by a source with co-ordinates $\mathbf{S}$, scattered by a rough acoustically rigid surface represented by the vector $\boldsymbol{\rho} = (x, y, \zeta(x, y, t))$ and recorded by a receiver with co-ordinates $\mathbf{M}$ is given by[14]

$$P(\mathbf{M}, t) = e^{-i\omega_a t} \int_\Sigma D_2(\theta_2(\boldsymbol{\rho}))$$
$$\times \, \mathbf{n}(\boldsymbol{\rho}) \cdot \nabla[D_1(\theta_1(\boldsymbol{\rho}))G_0(\boldsymbol{\rho}, \mathbf{S})G_0(\mathbf{M}, \boldsymbol{\rho})]d\boldsymbol{\rho}, \tag{7}$$

where ω_a is the frequency of the acoustic source transducer, Σ is the scattering surface, $\mathbf{n}$ is the normal to the scattering surface, and ∇ is the three-dimensional spatial gradient operator. The normal to the surface is described by

$$\mathbf{n} = \frac{\mathbf{e}_z - \nabla\zeta}{\sqrt{1 + |\nabla\zeta|^2}}, \tag{8}$$

where $\mathbf{e}_z$ is the unit vector in the z-direction, and $\nabla\zeta$ is the spatial gradient of the surface elevation ζ, with components only along the x- and y-directions. Equation (7) can be integrated over the plane (x, y) by changing to the co-ordinate $\boldsymbol{\rho}_0 = (x, y)$, with
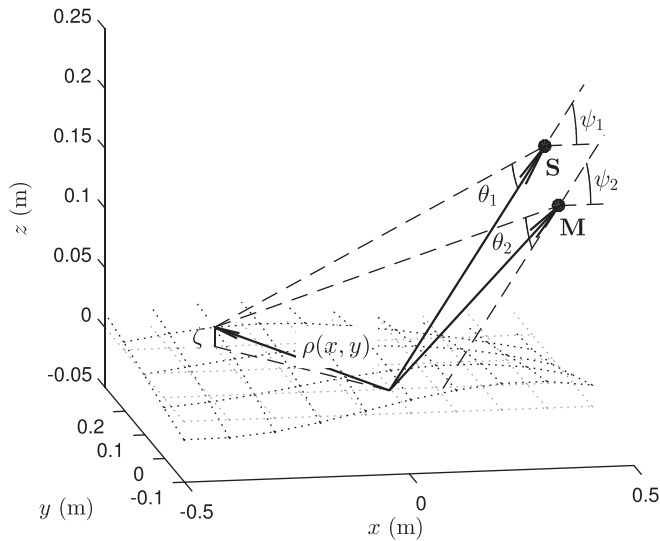

FIG. 2. Sketch of the geometry of the problem. The surface elevation ζ is defined with respect to the polar co-ordinate, $\boldsymbol{\rho}$. The angles θ_1 and θ_2 are measured from the axes of the transducer and of the microphone, respectively. The transducer and the microphone have the co-ordinates $\mathbf{S}$ and $\mathbf{M}$, and their axes are inclined by the angles ψ_1 and ψ_2 with respect to the horizontal plane, respectively.

$$d\boldsymbol{\rho}_0 = \sqrt{1 + |\nabla\zeta|^2}d\boldsymbol{\rho}. \tag{9}$$

The derivation of Eq. (7) is based on the assumption that both the receiver and the source are in the far field, $\kappa|\mathbf{M}| \gg 1$ and $\kappa|\mathbf{S}| \gg 1$. G_0 represents the free-field Green's function in three dimensions,[15]

$$G_0(\mathbf{r}_1, \mathbf{r}_2) = -\frac{1}{4\pi}\frac{e^{i\kappa|\mathbf{r}_1 - \mathbf{r}_2|}}{|\mathbf{r}_1 - \mathbf{r}_2|}, \tag{10}$$

where $\mathbf{r}_1$ and $\mathbf{r}_2$ are two generic vectors of co-ordinates. In a two-dimensional space, the Green's function is usually represented by its far field approximation, i.e.,

$$G_0(\mathbf{r}_1, \mathbf{r}_2) = \frac{i}{4}\sqrt{\frac{2}{\kappa\pi}}\frac{e^{i\kappa|\mathbf{r}_1 - \mathbf{r}_2| - i\pi/4}}{\sqrt{|\mathbf{r}_1 - \mathbf{r}_2|}}. \tag{11}$$

In this work, the average power Doppler spectrum of the scattered acoustic field is defined as[16]

$$S(\omega) = \frac{1}{T}\left\langle\left|\int_0^T P(\mathbf{M}, t)e^{i(\omega + \omega_a)t}dt\right|^2\right\rangle, \tag{12}$$

where the angular brackets represent averaging over a number of realizations, and ω is the Doppler frequency shift relative to the carrier acoustic frequency ω_a. In practice, the acoustic Doppler spectra were calculated with a discrete Fourier transform at the standard discrete set of frequencies, and the carrier frequency ω_a was then subtracted from these frequencies, so that the Doppler spectrum at the frequency $\omega = 0$ corresponded to the components of the signal with no Doppler shift. The scattered field $P(\mathbf{M}, t)$ was calculated based on the Kirchhoff approximation, according to Eq. (7). All terms of Eq. (7) were evaluated on a discretized rectangular spatial grid with grid separation Δr and with overall size L_x and L_y in the x- and y-direction, respectively. The integration was performed independently at a discrete set of instants, according to a frozen-surface approach.[16] The harmonic dependence with frequency ω_a was removed from the calculation of $P(\mathbf{M}, t)$ and of $S(\omega)$, as the two terms eventually cancel out. All geometric quantities and their gradients were calculated analytically at each location (x, y), based on known realizations of the random surface $\zeta(x, y, t)$ generated with the procedure that will be described in Sec. III B. The only exceptions were the directivity patterns D_1 and D_2 which were measured using the procedure described in Sec. II A, and the derivative $\partial D_1/\partial\theta_1$ which was calculated with a central finite difference scheme based on the measured $D_1(\theta_1)$. The average Doppler spectra were calculated according to Eq. (12), where the average was taken over 50 surface realizations.

B. Surface model

In order to calculate the Doppler spectrum based on Eq. (7), a set of realizations of the dynamic surface elevation $\zeta(x, y, t)$ was needed. Measurements of the probability distribution function of ζ in shallow turbulent flows suggest that

the statistics of the elevation are Gaussian, at least as a first approximation.[17,18] Realizations of a random surface with Gaussian statistics can be generated according to a linear random-phase model,[19] assuming that such a surface has a Fourier series representation, and that the coefficients of the series are mutually independent. According to such model, the statistics of the surface are completely characterized by its directional spectrum, $\Psi(k, \beta)$, and by the dispersion relation, $\Omega(k, \beta)$. A single realization of ζ is represented as

$$\zeta(x, y, t) = \sqrt{2} \sum_p \sum_q \xi_{pq} A(\mathbf{k}_{pq}) \cos[\mathbf{k}_{pq} \cdot \boldsymbol{\rho}_0 - \Omega(\mathbf{k}_{pq})t + \Phi_{pq}], \quad (13)$$

where $A(\mathbf{k}_{pq})$ is the surface amplitude spectrum defined as a function of the wavenumber vector $\mathbf{k}_{pq}$ with components $k_p \cos(\beta_q)$ and $k_p \sin(\beta_q)$, where p and q are indices, $\Omega(\mathbf{k}_{pq}) = \Omega(k_p, \beta_q)$ is the frequency of the waves with wavenumber $\mathbf{k}_{pq}$ determined by the dispersion relation, $\boldsymbol{\rho}_0$ is a polar co-ordinate with components x and y, ξ_{pq} is a random normally distributed variable, and Φ_{pq} is a random variable with uniform distribution in the interval between $-\pi$ and π. The relation between the amplitude spectrum of the surface elevation $A(\mathbf{k}_{pq})$ in Eq. (13) and its directional spectrum $\Psi(k, \beta)$ is expressed by

$$\sum_p \sum_q A^2(\mathbf{k}_{pq}) = \int_0^\infty \int_0^{2\pi} \Psi(k, \beta) k \, dk \, d\beta = \sigma^2, \quad (14)$$

where σ is the standard deviation of the surface elevation.

While there are models that predict the directional spectrum of ocean waves accurately and in a variety of conditions,[20] a general form of the same spectrum that is valid in shallow turbulent flows has not been determined yet, especially for the short capillary waves which are of larger importance for the acoustic Doppler spectra. The direct estimation of the surface directional spectrum based on the measurement of the frequency spectrum cannot be obtained when the flow velocity is of a similar order of magnitude as the group and phase velocity of the waves on the surface.[21] For the streamwise wavenumber spectrum of waves generated by grid turbulence in a flow, Savelsberg and Van De Water[22] proposed a power-function spectrum with a very steep decay, proportional to k^{-8}. In shallow turbulent flows over a rough bed, Horoshenkov et al.[17] suggested a Gaussian quasi-harmonic shape of the correlation function, which indicates a rapidly decaying Gaussian spectrum of the elevation.

For this study, it was decided to adopt the power-function spectrum $\Psi(k) \propto k^{-\alpha}$ proposed by Savelsberg and van de Water.[22] Power-function spectra are commonly used in models of the ocean waves, at least as a fundamental kernel,[20] and they have been linked to the wave turbulence phenomenon.[23] The measurement of the spectrum slope α is difficult to achieve, especially for the larger wavenumbers which have a dominant role on backscattering. The numerical simulations were performed with two different values of the spectrum slope, $\alpha = 5$ and $\alpha = 7$, respectively. In this way the effects of α on the acoustic Doppler spectra could be

quantified. The two values of α used for this work were chosen arbitrarily, but they seemed to represent the range of values that approximated the measured Doppler spectra more accurately.

The dependence of the angular spectrum on the angle β is commonly expressed in terms of an angular distribution $\mathcal{D}$,[24] which is in general a function of k, i.e.,

$$\Psi(k, \beta) = \Psi(k)\mathcal{D}(k, \beta) \propto k^{-\alpha}\mathcal{D}(k, \beta), \quad (15)$$

where $\Psi(k)$ represents the factor of $\Psi(k, \beta)$ which is independent of the direction of propagation. Dolcetti et al.[11] found that the only waves propagating at an angle β different from zero at a range of shallow turbulent flow conditions were gravity waves with the wavenumber k_0 and with the dispersion relation represented by Eq. (4). Therefore, in the simulations of the dynamic surface the angular distribution was represented by

$$\mathcal{D}(k, \beta) = \begin{cases} \tilde{\mathcal{D}}(\beta), & \text{where } k = k_0, \\ \tilde{\mathcal{D}}(\beta)[\delta(\beta) + \delta(\beta - \pi)], & \text{where } k \neq k_0, \end{cases} \quad (16)$$

where δ is a delta function. This representation ensured the continuity of the angular spectrum at the wavenumber k_0 and at the angles $\beta = 0$ and $\beta = \pi$.

The waves with wavenumber k_0 also corresponded to the longest waves observed in Ref. 11, at all conditions where the mean surface velocity was larger than the minimum phase velocity of gravity-capillary waves in still water, equal to approximately 0.23 m/s. Because these relatively long waves have little effect on the backscattered Doppler spectra when nonlinear interactions among waves are neglected, it is expected that the choice of the distribution would affect the results of the model only marginally. Hence, it was decided to implement two standard distributions which have had large applications for the simulation of oceanic waves,[24] namely, the so-called Poisson distribution,

$$\tilde{\mathcal{D}}_p(\beta) = \frac{1}{2\pi} \frac{(1 - b^2)}{[1 - 2b\cos(\beta - \pi) + b^2]}, \quad (17)$$

and the sech^2 distribution

$$\tilde{\mathcal{D}}_s(\beta) = \frac{1}{\tan(b\pi)} \frac{b}{2\cosh^2[b(\beta - \pi)]}. \quad (18)$$

These distributions do not necessarily apply to the waves over shallow turbulent flows, but they have been chosen because of their relatively easy experimental characterization,[24] so that their applicability may be verified in future investigations. Performing the simulations with two different distributions also allows the empirical evaluation of the effects of the angular distribution on the acoustic Doppler spectra.

The coefficient b in both angular distributions was chosen in such a way that $\tilde{\mathcal{D}}(\pi) = 10^{1.5}\tilde{\mathcal{D}}(0)$. This was in agreement with the measurements of the frequency-wavenumber spectra of the elevation reported in Ref. 11, which showed that the spectrum of the waves with wavenumber k_0

J. Acoust. Soc. Am. **142** (6), December 2017

Dolcetti et al.   3391

propagating against the current was approximately 1.5 orders of magnitude larger than that of the waves with the same wavenumber propagating downstream. As a result, b was equal to 0.698 for the Poisson distribution, and to 0.768 for the sech^2 distribution. The independence from the wavenumber k of the function $\tilde{\mathcal{D}}$ as defined in Eq. (16) means that the same relation between the amplitude of waves propagating in opposite direction was extrapolated to arbitrary wavenumbers in this study.

Savelsberg and van de Water[22] measured the dispersion relation of the waves in a flow where turbulence was generated by either active or passive grids. These authors identified waves following both dispersion relations given in Eqs. (4) and (5). The first of these equations is representative of gravity-capillary waves, while the non-dispersive relation of Eq. (5) represents waves that are rigidly advected by the mean surface velocity. These results were confirmed by the experiments of Dolcetti et al.[11] in shallow turbulent flows with a rough bed, although Dolcetti et al. observed the non-dispersive types of waves only at the flow conditions where the mean surface velocity was smaller than the minimum phase velocity of gravity-capillary waves in still water. In this work it was assumed that both dispersive and non-dispersive waves coexist at all flow conditions. This was motivated by the experimental results presented in Sec. IV, which show that a Doppler peak at the frequency of approximately $\omega = \Omega_U(k_B)$ exists in all the measured Doppler spectra.

The non-dispersive waves were assumed to be represented by the same form of the angular spectrum of Eq. (15), but to propagate only downstream at the angle $\beta = 0$. At the only flow condition where these waves were observed, Dolcetti et al.[11] found that their spectrum was two to three times larger than that of the waves propagating downstream. In the model described here, the spectrum of the non-dispersive waves was set 2.5 larger, therefore intermediate between that of the downstream- and upstream-propagating gravity-capillary waves at all wavenumbers.

Based on the above discussion, the realizations of the random surface $\zeta(x, y, t)$ were generated according to Eq. (13). Introducing the new variable $k_j = k_p \cos(\beta_q)$, approximating the two sums in Eq. (13) with integrals of a continuous spectrum, and taking advantage of the properties of the delta functions in Eq. (16), it is possible to remove one of the two summations of Eq. (13) by integrating over the transverse component of the wavenumber. Then, $\zeta(x, y, t)$ can be defined by two distinct sums, one for the waves with the constant wavenumber modulus $k_p = k_0$ and with the angle of propagation defined by

$$\beta_j = \sin^{-1}\left[\sqrt{1 - \left(\frac{k_j}{k_0}\right)^2}\right], \tag{19}$$

and another one for the waves with the wavenumber modulus $k_p > k_0$ which propagate only parallel to the x-direction, with $\beta_q = 0$ or $\beta_q = \pi$. As a result, $\zeta(x, y, t)$ can be calculated as

$$
\begin{aligned}
\zeta(x, y, t) = \sqrt{2} \sum_{|k_j| < k_0, j=1}^{N} A_{\beta,j} &\left\{ \xi_j \sqrt{\tilde{\mathcal{D}}(\beta_j)} \cos\left[k_0 \cos(\beta_j)x + k_0 \sin(\beta_j)y - \Omega_w(k_0, \beta_j)t + \Phi_j\right] \right. \\
&+ \xi_j \sqrt{\tilde{\mathcal{D}}(\beta_j)} \cos\left[k_0 \cos(\beta_j)x - k_0 \sin(\beta_j)y - \Omega_w(k_0, \beta_j)t + \Phi_j\right] \\
&+ \xi_j \sqrt{\tilde{\mathcal{D}}(\pi - \beta_j)} \cos\left[-k_0 \cos(\beta_j)x + k_0 \sin(\beta_j)y - \Omega_w(k_0, \pi - \beta_j)t + \Phi_j\right] \\
&\left. + \xi_j \sqrt{\tilde{\mathcal{D}}(\pi - \beta_j)} \cos\left[-k_0 \cos(\beta_j)x - k_0 \sin(\beta_j)y - \Omega_w(k_0, \pi - \beta_j)t + \Phi_j\right] \right\} \\
&+ \sqrt{2} \sum_{|k_j| \geq k_0, j=1}^{N} A_{\alpha,j} \left\{ \xi_j \sqrt{\tilde{\mathcal{D}}(0)} \cos\left[k_j x - \Omega_w(k_j, 0)t + \Phi_j\right] \right. \\
&\left. + \xi_j \sqrt{\tilde{\mathcal{D}}(\pi)} \cos\left[-k_j x - \Omega_w(k_j, \pi)t + \Phi_j\right] + \xi_j \sqrt{1.5\tilde{\mathcal{D}}(0)} \cos\left[k_j x - \Omega_U(k_j, 0)t + \Phi_j\right] \right\}.
\end{aligned}
\tag{20}
$$

The first two terms dependent on β_j in Eq. (20) represent waves that propagate downstream, with opposite signs of the transverse wavenumber $k_0 \sin(\beta_j)$, while the third and last terms indicate waves that propagate upstream. The amplitude spectrum of these waves is given by

$$A_{\beta,j} = A_0 \left[\sqrt{2} \sin(\beta_j)\right]^{-1}, \tag{21}$$

where A_0 is a normalization factor that ensures that Eq. (14) is satisfied. The three additional terms of Eq. (20) with the amplitude spectrum defined by

$$A_{\alpha,j} = A_0 \left(\frac{k_j}{k_0}\right)^{-\alpha/2}, \tag{22}$$

represent gravity-capillary waves that propagate downstream with the angle $\beta_q = 0$, gravity-capillary waves that

propagate upstream with the angle $\beta_q = \pi$, and non-dispersive waves that propagate at the same velocity of the flow, respectively. The normalization factor A_0 is defined as

$$A_0 = \sigma \sqrt{\frac{\Delta k}{k_0}}$$
$$\times \left\{ \frac{1}{2} + \frac{[2.5\tilde{\mathcal{D}}(0) + \tilde{\mathcal{D}}(\pi)]}{1 - \alpha} \left[\left(\frac{k_N}{k_0}\right)^{(1-\alpha)} - 1 \right] \right\}^{-1/2}, \tag{23}$$

where k_N is the wavenumber of the shortest modeled waves, and Δk is related to the size of the modeled surface by $\Delta k = 2\pi/L_x$, $k_j = j\Delta k$, $j = 1, \ldots, N$. It is understood that ξ_j and Φ_j, which have the same meaning of ξ_{pq} and Φ_{pq} but are defined based on a single index, represent an independent realization of random variables every time they appear in Eq. (20), so that the amplitude and phase of each term are random and independent. The effect of the maximum wavenumber k_N on the simulations is discussed in Sec. III C.

C. Numerical computation

The surface realizations were generated with the expansions represented by Eqs. (20)–(23) at the same discrete set of locations and the same set of discrete time intervals used for the calculation of the scattered field $P(\mathbf{M}, t)$. Two-dimensional surface realizations were obtained with the same method, imposing $y = 0$. The spatial grid used for all simulations had the size $\Delta r = \lambda_a/25 = 0.32$ mm, where $\lambda_a = 2\pi/\kappa$ was the acoustic wavelength. For the two-dimensional simulations, the computational domain had the size $L_x = 2$ m, and the evolution of the surface was simulated during a period of one second, with the time step $\Delta t = 1$ ms. Because of computational memory constraints, in the three-dimensional simulations $L_x = 1.5$ m, $L_y = 0.5$ m, $\Delta t = 2$ ms, and the duration of the simulations was 0.25 s.

The convergence of the simulation with respect to L_x and Δr was tested on a single realization of the Doppler spectrum obtained for a two-dimensional surface with the standard deviation $\sigma = 1.21$ mm, the characteristic wavenumber $k_0 = 47.0$ rad/m, and the characteristic frequency $k_0 U_0 = 21.6$ rad/s. The parameters of this surface corresponded to those of flow condition 7, which had an intermediate value of the Froude number, $F = 0.54$, and therefore it was expected to be representative of the average behavior of the surface. The convergence parameter was defined as the integral over frequency of the absolute difference between the Doppler spectra obtained with different grid parameters. This value changed by 2.3% when the grid size was reduced from $\lambda_a/25$ to $\lambda_a/50$, and by 1.1% when the size of the rough surface was increased from 2 to 4 m. In both cases, no qualitative change to the shape of the simulated Doppler spectra was observed.

All simulations in this work relied upon the validity of the Kirchhoff approximation, for the specific surface characteristics and geometry of the measurement setup. The validity of this approximation, represented by Eq. (6), was

checked in all two-dimensional simulations. The radius of curvature R_c was calculated numerically as

$$R_c = \left[1 + \left(\frac{d\zeta}{dx}\right)^2 \right]^{3/2} \left| \frac{d^2\zeta}{dx^2} \right|^{-1}. \tag{24}$$

The characteristic angle $\psi = 30°$ was used for the calculation of Eq. (6). In the range of conditions investigated here, the minimum of the Kirchhoff parameter was found to be approximately 2.2 for a surface with the same parameters as those measured at flow condition 5, which had a relatively rougher surface with a larger characteristic slope $k_0\sigma = 0.08$ The root mean squared amplitude of the Kirchhoff parameter at the same condition was 3.4×10^3. These values are believed to be sufficient for the applicability of the Kirchhoff approximation at this condition,[25] and therefore at all remaining flow conditions where the Kirchhoff parameter was larger.

A further validation of the model was performed by comparison with a standard boundary elements method (BEM),[26] for a single realization of a surface with the same characteristic parameters as the roughest condition 5. The BEM model was developed based on the same boundary conditions used for the Kirchhoff model.[14] The simulated Doppler spectra obtained with BEM and with the Kirchhoff approximation are shown in Fig. 3. The relative difference between these spectra was calculated as the integral over frequency of their absolute difference, divided by the integral of the Kirchhoff Doppler spectrum, and was equal to 5.3%. The spectrum obtained with the BEM is qualitatively identical to that obtained with the Kirchhoff approximation. At the other flow conditions, where the Kirchhoff parameter was larger, the difference between the two models is expected to be smaller. The considerably shorter computational time (approximately 100 times less) required by the model based on the Kirchhoff approximation motivated the use of this model for all calculations reported here.

The validity of the surface model used for this study was checked by comparing the average frequency spectrum
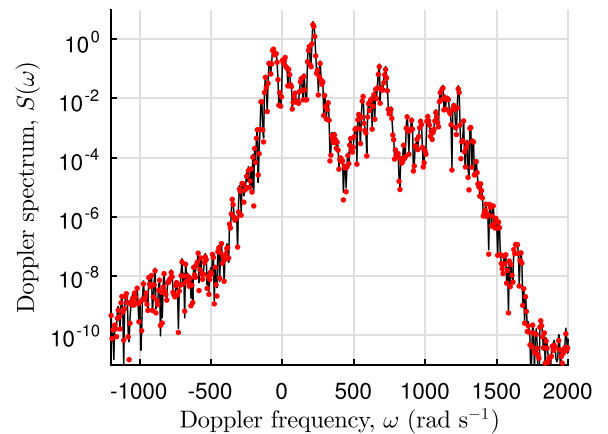

FIG. 3. (Color online) Examples of one realisation of the simulated Doppler spectrum, obtained (black line) with the model based on the Kirchhoff approximation, and (red dots) with the Boundary Elements Method. The predictions by the two models are practically indistinguishable.

and zero time-lag correlation function of ζ with the measurements of the same quantities presented in Ref. 11, for similar parameters of the water surface. This comparison is illustrated in Figs. 4(a), and 4(b), respectively, for the intermediate Froude number flow condition 7. In spite of the apparently arbitrary choice of the shape of the directional spectrum, the model was able to represent the main characteristics of the frequency spectra and of the correlation function as they were identified in Ref. 11, namely, the increase of slope of the frequency spectrum above the frequency $k_0 U_0$, and the fluctuation of the zero time-lag spatial correlation function with the period $2\pi/k_0$. The measured frequency spectrum at condition 7 with an intermediate Froude number [Fig. 4(a)] appears to be better approximated by $\alpha = 5$, particularly for higher frequencies. This behavior was not representative of the spectra at all conditions, and the slope of the frequency spectrum was found to depend on the Froude number, as observed in Ref. 11.

As stated in Sec. II A, the Bragg scattering mechanism provides a direct link between the acoustic Doppler spectra and the behavior of the Bragg-resonant surface waves with the wavenumber k_B. The velocity of the flow near the surface can be estimated from the frequency of the Bragg peaks, and the amplitude and width of these peaks can be linked to the statistics of the surface waves with wavenumber k_B.[3] If the measurements are performed outside of the Fraunhofer zone,

the scattering occurs from a range of different directions, and a single Bragg frequency does not exist. According to the simulations obtained with the Kirchhoff model, the acoustic Doppler spectra can still be interpreted in terms of Bragg scattering, if one refers to the direction of the maximum directivity of the transducer in order to calculate the wavenumber that satisfies the Bragg resonance condition [like in Eq. (2)]. This is demonstrated in Fig. 5, which compares the average Doppler spectra simulated with different values of the maximum wavenumber k_N for the rough surface. The results shown in Fig. 5 were obtained with the two-dimensional version of the model, based on the surface parameters measured at the intermediate Froude number condition 7, with $\alpha = 5$. The shortest waves existing on the surface had the wavelength $2\pi/k_N$, where the wavenumber k_N was varied between $2\pi/0.006$ rad/m and $2\pi/0.003$ rad/m. When $k_N = 2\pi/0.006$ rad/m, the Doppler spectrum in Fig. 5 decays rather smoothly away from a central peak at the frequency $\omega = 0$. This peak is related to the almost specular reflections of the acoustic waves which occur right below the transducer, where the amplitude of the incident acoustic field is determined by the value of the directivity D_1 at the angle $\theta_1 = 2\pi/3 = \pi - \psi_1$ [Eq. (1)]. This value was found to be equal to 0.05% of the maximum directivity. Although very small, the specular reflection of the incident field can cause a finite value of the average scattered field at the frequency ω_a,[27] which is independent of the surface velocity, and has no Doppler shift, $\omega = 0$. At small non-zero Doppler frequencies and for a moving rough surface, the amplitude of the Doppler spectrum varies smoothly with the frequency, and the width of the central peak is governed by the roughness of the surface relative to the acoustic wavelength.[1] These phenomena are discussed with more detail in Ref. 36.

Bragg scattering is expected to cause peaks of the Doppler spectrum at the frequencies $\Omega(k_B, 0)$ and $\Omega(k_B, \pi)$, where Ω is representative of any of the dispersion relations of Eqs. (4) or (5). The increase of k_N near and above k_B
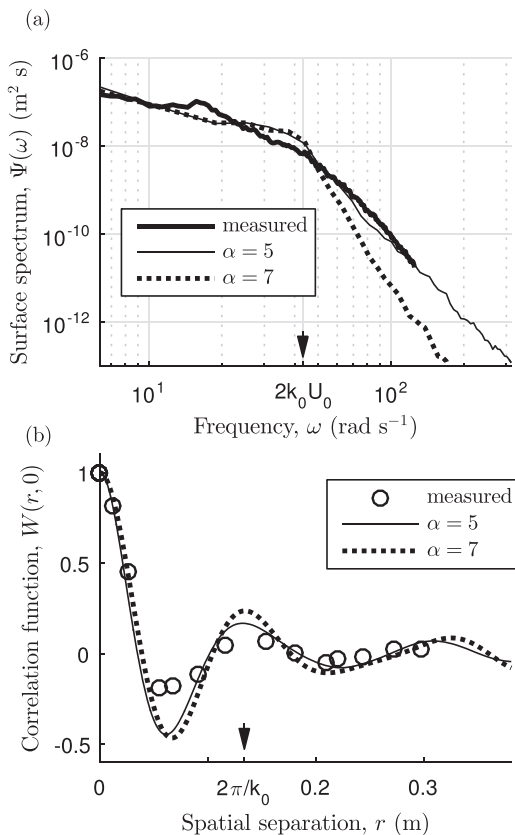

FIG. 4. Examples of (a) the frequency spectrum and (b) the zero time-lag correlation function of the surface elevation. Thick line and circles, measurements; thin lines, calculated for the modeled free surface, with different slopes of the surface spatial spectrum, α. The frequency spectrum and the correlation function scale with the characteristic frequency $2k_0 U_0$ and with the wavelength $2\pi/k_0$ of the stationary waves, indicated by the arrows.
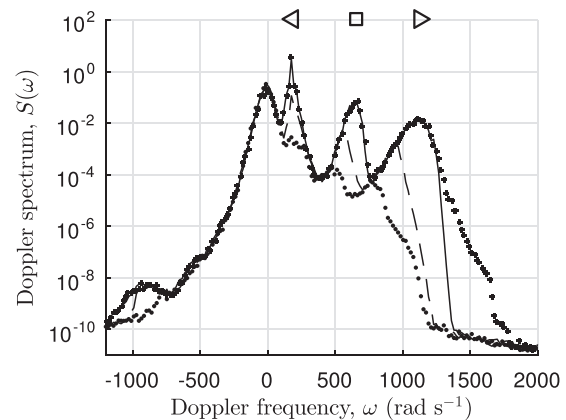

FIG. 5. Examples of the simulated Doppler spectrum, with increasing maximum wavenumber k_N of the modeled rough surface. Dots, $k_N = 2\pi/0.006$ rad/m; dashed, $k_N = 2\pi/0.005$ rad/m; solid, $k_N = 2\pi/0.004$ rad/m; crosses, $k_N = 2\pi/0.003$ rad/m. The symbols on top indicate the frequencies of the Bragg-resonant waves with wavenumber k_B: ($\triangleleft$) upstream- and ($\triangleright$) downstream-propagating capillary waves, and ($\square$) non-dispersive waves. Peaks of the simulated Doppler spectra appear when k_N is larger than the wavenumber that satisfies the Bragg resonance condition, $k_B = 2\pi/0.0044$ rad/m.

caused the gradual growth of three peaks of the Doppler spectrum, occurring at the three frequencies $\Omega_w(k_B, \pi)$ = 181 rad/s, $\Omega_U(k_B, 0)$ = 657 rad/s, and $\Omega_w(k_B, 0)$ = 1133 rad/s, which represent gravity-capillary waves propagating upstream, non-dispersive waves, and gravity-capillary waves propagating upstream, respectively. These frequencies are indicated by the symbols on the top of Fig. 5. In turn, the amplitude of the peak near $\omega = 0$ remained constant. The peaks stopped growing when k_N was larger than $2\pi/0.004$ rad/m, which demonstrates that they were governed by the presence of the Bragg-resonant waves with $k_B = 2\pi/0.0044$ rad/m. The predominance of Bragg scattering at the conditions used for this work allows for the estimation of the mean surface velocity based on the peaks of the Doppler spectra, as demonstrated, for example in Ref. 6. The behavior of the short Bragg-resonant capillary waves can also be inferred from the behavior of these peaks. Based on the results shown in Fig. 5, all the following simulations were performed with $k_N = 2\pi/0.003$ rad/m, since a further increase of k_N reduced the applicability of the Kirchhoff approximation.

The effects of the three-dimensionality of the surface corrugation are investigated in Fig. 6. This figure shows the comparison of the Doppler spectra obtained for four types of simulations, namely, (i) a two-dimensional simulation with the Poisson angular distribution [Eq. (17)], (ii) a two-dimensional simulation with the sech^2 distribution [Eq. (18)], (iii) a three-dimensional simulation with the Poisson angular distribution, and (iv) a three-dimensional simulation with the Poisson angular distribution based on a broad spectrum representation. This was obtained by removing the delta functions from the definition of the angular distribution in Eq. (16), so that the same angular distribution $\tilde{\mathcal{D}}(\beta)$ was applied to all waves, regardless of their wavenumber. In this way, also the waves with the wavenumber close to k_B were allowed to propagate at an angle with respect to the x-direction.

All simulations shown in Fig. 6 were performed with the same surface parameters obtained for the intermediate
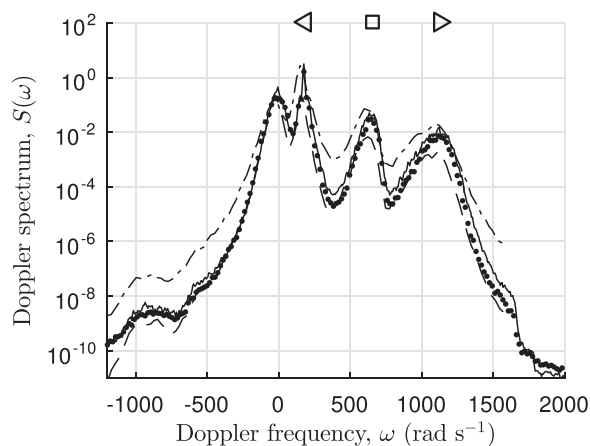

FIG. 6. Examples of the simulated Doppler spectrum calculated with different dependence of the spectrum of the surface waves on their direction of propagation. Solid, two-dimensional surface, Poisson distribution [Eq. (17)]; dots, two-dimensional surface, sech^2 distribution [Eq. (18)]; dashed, three-dimensional surface, narrow spectrum (dashed-dotted), three-dimensional surface, broad spectrum.

Froude number flow condition 7, and with $\alpha = 5$. The four spectra are very similar to each other, with the exception of the one obtained with a three-dimensional simulation using a broad surface spectrum, in which case the scattering from different angles increased the amplitude of the Doppler spectrum, mainly at the frequencies in between the three Bragg peaks. The similarity between the various spectra suggests that the main contribution to the Doppler spectra comes from the waves with the wavefront perpendicular to the x-direction, although the widening of the spectral distribution effectively increases the width of the spectral peaks due to the relatively wide directivity pattern. It should be noted that the angular distribution employed for the broad-spectrum three-dimensional simulation shown in Fig. 6 is in contrast with the measurements of the surface spectra at low wavenumbers reported in Ref. 11, and that the angular distribution of the capillary waves with the wavenumber close to k_B has not yet been determined. A broadening of the peaks of the Doppler spectra is known to occur also due to nonlinear interactions among surface waves,[28] or to the modulation of the velocity of the surface waves caused by the turbulent flow.[6] Unfortunately it is not possible to quantify the relative importance of each of these phenomena due to the lack of surface models of practical use which include all these effects and which apply to turbulent flows. Therefore, and in light of the considerably larger computational time required for the three-dimensional simulations, all the following numerical results were based on two-dimensional simulations with the Poisson angular distribution. These were believed to be sufficient to illustrate the behavior of the acoustic Doppler spectra, at least qualitatively.

IV. EXPERIMENTAL RESULTS

Three representative examples of the measured Doppler spectra are shown in Fig. 7, together with the corresponding results of the two-dimensional simulations based on the Kirchhoff approximation, obtained with $\alpha = 5$ and $\alpha = 7$, respectively. These examples were obtained for three different flow conditions with a low Froude number [$F = 0.41$, condition 2, Fig. 7(a)], with an intermediate Froude number [$F = 0.54$, condition 7, Fig. 7(b)], and with a higher Froude number [$F = 0.61$, condition 10, Fig. 7(c)], respectively. In all cases, the simulations approximate the behavior of the spectra well at the frequency near $\omega = 0$. This region of the spectra shows a main peak which is governed by the near-specular reflections occurring below the source and the microphone, and which is mainly affected by the slow dynamics of relatively long waves on the surface.[1,29] The ability of the simulations to represent this region of the Doppler spectra demonstrates the validity of the dynamic model of the surface at the larger scales, where more accurate information about the surface dynamics was available.

At high Doppler frequencies, the simulated spectra show the three peaks that have been related to the Bragg-resonant waves, at the three frequencies $\Omega_w(k_B, \pi)$, $\Omega_U(k_B, 0)$, and $\Omega_w(k_B, 0)$. These three frequencies are indicated by the symbols at the top of Fig. 7, for each flow condition. At the low Froude number condition, represented in Fig.

J. Acoust. Soc. Am. **142** (6), December 2017
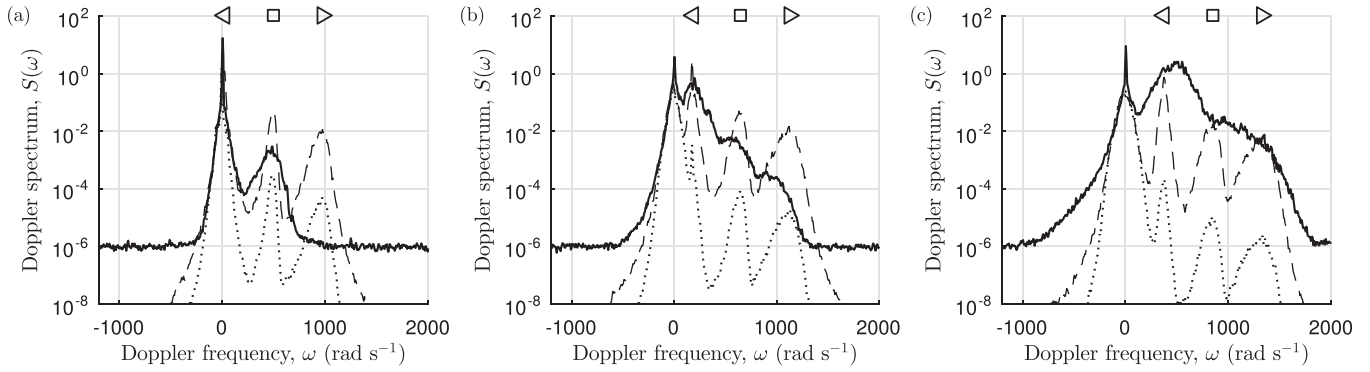
Dolcetti et al.   3395

FIG. 7. Examples of Doppler spectra, for three flow conditions with (a) lower Froude number (flow condition 2), (b) intermediate Froude number (flow condition 7), and (c) higher Froude number (flow condition 10). Simulated, with different slope of the surface spatial spectrum, (dashed) $\alpha = 5$, (dotted) $\alpha = 7$, compared to experimental measurements (solid). The symbols on top indicate the frequencies of the Bragg-resonant waves with wavenumber k_B: ($\triangleleft$) upstream- and ($\triangleright$) downstream-propagating capillary waves, and ($\square$) non-dispersive waves propagating with the velocity of the flow.

7(a), the frequency of the upstream-propagating Bragg-resonant waves is $\Omega_w(k_B, \pi) = 24.1$ rad/s, and the corresponding peak is shaded by the main peak centered in $\omega = 0$. The amplitude of the three peaks decreases with the increase of the spectrum slope α. The intermediate peak represents the non-dispersive waves that propagate at the speed of the mean surface velocity, according to Eq. (5). This peak is clearly visible in the measured spectra at the low [Fig. 7(a)] and intermediate [Fig. 7(b)] Froude number conditions, at the frequencies of 500 and 657 rad/s, respectively. At the higher Froude number condition [Fig. 7(c)] this peak is expected at the frequency of 857 rad/s, where it appears to be partly shaded by another peak at lower frequency. Non-dispersive waves had only been observed in Ref. 11 at the flow conditions where the mean surface velocity was smaller than the minimum phase velocity of gravity-capillary waves, which is approximately 0.23 m/s. The results shown in Fig. 7 suggest that non-dispersive waves are always present at the surface of shallow turbulent flows over a wide range of wavenumbers, although the limited resolution of the measurements reported in Ref. 11 and the closeness of the three dispersion relations at the smaller wavenumbers may have made them difficult to detect at most conditions described in that study.

In contrast, the two peaks that correspond to capillary waves propagating upstream and downstream with frequencies $\Omega_w(k_B, 0)$ and $\Omega_w(k_B, \pi)$, respectively, cannot be seen in the measured Doppler spectra for the low Froude number condition [Fig. 7(a)], although they were predicted by the model. These two peaks are more clearly visible at the intermediate Froude number condition [Fig. 7(b)] and they are larger at the higher Froude number condition [Fig. 7(c)], where they effectively shade the intermediate non-dispersive peak. Gravity waves propagating downstream were observed at all flow conditions by Dolcetti et al.,[11] including the low Froude number condition 2, while the upstream propagating waves were found only at higher Froude numbers. It should be noted that these observations were done at wavenumbers much smaller than k_B. The progressive growth of the peaks at the Bragg frequencies $\Omega_w(k_B, 0)$ and $\Omega_w(k_B, \pi)$ can be interpreted based on the results shown in Figs. 5 and 6, where the amplitude of the peaks was found increasing with the shift of the cut-off wavenumber of the surface spectrum,

and with the broadening of the angular distribution of the surface waves. It is suggested that a similar increase of the cut-off wavenumber, or the broadening of the angular distribution, also occurred between the three conditions represented in Fig. 7.

At all the measured conditions where the peak of the upstream propagating waves at the frequency $\Omega_w(k_B, \pi)$ was observed, this peak had the amplitude larger than that of other waves propagating downstream. The asymmetry of the Doppler spectrum had already been observed by Plant et al.[6] At the low and intermediate Froude number conditions [Figs. 7(a) and 7(b)], the amplitude of the measured Doppler peaks is intermediate between the model predictions obtained with $\alpha = 5$ and $\alpha = 7$. At the higher Froude number condition [Fig. 7(c)], the simulation with $\alpha = 5$ approximates the measurements better than that with $\alpha = 7$. These observations must be interpreted carefully. Even assuming the validity of the power-function decay of the surface spectrum, it seems unlikely that the spectrum slope remains unchanged in both the gravity- and the capillary-dominated ranges of scales, because of the different physical phenomena involved. Because of the predominance of Bragg scattering, very little can be said about the surface spectrum at the intermediate scales based on the observations of Fig. 7 alone. It is suggested, instead, that α can be representative of the amplitude of the short capillary waves with the wavenumber k_B, relative to that of the longer waves with the wavenumber k_0. In this sense, the results of Fig. 7 suggest that the amplitude of these short waves became increasingly larger with respect to the characteristic amplitude of the surface fluctuations when the Froude number increased. Across the whole set of tested flow conditions, the ratio k_B/k_0 varied between 11.8 and 52.6. Assuming α to be between 5 and 7, it is suggested that the waves with wavenumber k_B had the amplitude between 500 times and 10^5 times smaller than the characteristic wave amplitude σ, which was on the order of 1 mm. Even smaller waves are capable of producing larger Doppler peaks if their angular spectrum is broad, as shown in Fig. 6. Such very small waves are extremely difficult to measure directly with means alternative to acoustic.

At all conditions represented in Fig. 7, the peaks of the measured spectra are considerably wider than those

predicted by the model, to the point that the intermediate non-dispersive peak is not distinguishable from the measured spectrum of Fig. 7(c) alone, without the aid of the simulated spectrum. As demonstrated in Fig. 6, wider spectral peaks can be caused by a broad angular spectrum of the capillary waves on the surface. Alternatively, the widening of the Doppler peaks is usually interpreted as a manifestation of higher-order nonlinear interactions among surface waves with different scales,[28,30] or as the result of turbulent fluctuations of the surface velocity.[6] To be able to determine the cause of the wide peaks of the Doppler spectra uniquely, one would need to measure the angular spectrum of the short and small capillary waves on the surface, or to model the nonlinear interactions among waves, and between the waves and the flow. These interactions cannot be modeled with a linear random phase model of the surface. For so-called two-scale scattering models,[31,32] they can be taken into account with a set of modulation transfer functions,[28,33] or by modeling the statistics of the velocity field induced by the wave system,[6] although only when the Fraunhofer zone approximation applies. More sophisticated weakly nonlinear hydrodynamic models that resolve the temporal evolution of the sea surface have been employed in Monte Carlo simulations of back-scattered Doppler.[30,34] None of the known nonlinear surface models of practical use apply to capillary waves over a turbulent shallow flow with a roughened bed, when the surface velocity is larger than the minimum phase velocity of the gravity-capillary waves and it is subject to turbulent fluctuations. More appropriate models of the surface dynamics need to be developed in order to improve the accuracy of the predictions at the flow conditions typical of shallow turbulent flows.

The behavior of the measured Doppler spectra appears to be consistent within separate ranges of flow conditions. Figure 8 represents the measured Doppler spectra across the whole range of flow conditions. The abscissa in this figure is the non-dimensional frequency $\omega/\Omega_U(k_B, 0)$, which is equal to one at the frequency of the non-dispersive waves with wavenumber k_B. To facilitate the visualization of the data, the various flow conditions have been grouped into four groups, each representative of a specific range of Froude numbers. Conditions 1 to 4 have the lower Froude numbers smaller than 0.49. Conditions 5 to 8 had the intermediate Froude numbers between 0.49 and 0.57. Conditions 9 to 13 had the larger Froude numbers, larger than 0.57.

All conditions in the three groups represented in Fig. 8(a), 8(b), and 8(c) behave similarly to the already discussed conditions 2 [Fig. 7(a)], 7 [Fig. 7(b)], and 10 [Fig. 7(c)], respectively, which had similar values of the Froude number. Specifically, the Doppler spectra measured at the low Froude number conditions shown in Fig. 8(a) have a clear peak at the frequency of the non-dispersive Bragg-resonant waves, $\Omega_U(k_B, 0)$. At these conditions, there is no evidence of dispersive capillary waves propagating either upstream, or downstream. With the increase of the Froude number, at the conditions shown in Fig. 8(b), there is an increase of the Doppler spectrum at the frequency $\Omega_w(k_B, 0)$, which indicates the presence of downstream-propagating Bragg-resonant capillary waves. A large peak at the frequency
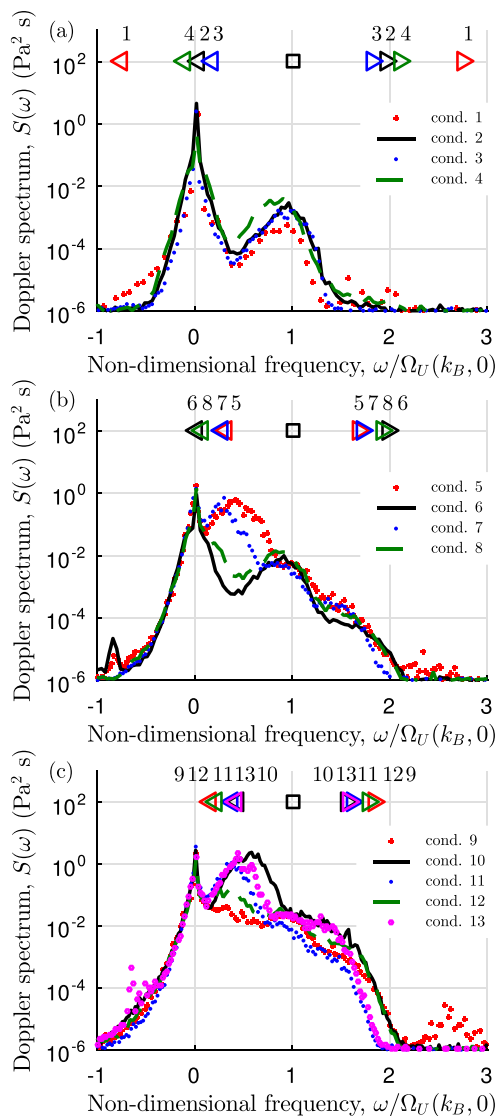

FIG. 8. (Color online) Measured Doppler spectra, at (a) low Froude number conditions, (b) intermediate Froude number conditions, and (c) higher Froude number conditions. The Doppler frequency ω is non-dimensionalized with respect to the frequency of the non-dispersive Bragg-resonant waves with wavenumber k_B propagating at the same velocity of the flow, $\Omega_U(k_B, 0)$. The symbols on top indicate the non-dimensional frequency of the Bragg-resonant waves: ($\triangleleft$) upstream-propagating and ($\triangleright$) downstream-propagating capillary waves, and ($\square$) non-dispersive waves. The colors and numbers indicate the corresponding flow conditions. The non-dimensional frequency of the non-dispersive waves is the same for all flow conditions.

$\Omega_w(k_B, \pi)$ of upstream-propagating Bragg-resonant capillary waves is also observed in Fig. 8(b), but only at the flow conditions 5 and 7. The frequency $\Omega_w(k_B, \pi)$ was very close to zero in the other flow conditions 6 and 8, therefore the peak of the upstream-propagating waves may have been shaded by the main peak at zero frequency at these flow conditions. The effects of dispersive capillary waves appears to increase further at higher Froude numbers, as shown in Fig. 8(c). In this figure, the amplitude of the Doppler spectra at the frequency $\Omega_w(k_B, 0)$ of downstream-propagating Bragg-resonant waves is close to the amplitude of the same spectra at the frequency $\Omega_U(k_B, 0)$ of the non-dispersive waves, so that

the peak at the latter frequency is almost impossible to recognize. The peak at the frequency $\Omega_w(k_B, \pi)$ of the upstream-propagating Bragg-resonant waves is again only visible at the flow conditions 10, 11, and 13. At the remaining flow conditions 9 and 12, $\Omega_w(k_B, \pi)/\Omega_U(k_B, 0)$ was smaller than 0.25, and the peak may have been shaded by the large spectral peak near $\omega = 0$.

To provide a quantitative metric of the shape of the measured Doppler spectra shown in Fig. 8, Fig. 9 shows the amplitude of these spectra measured at the three frequencies of the Bragg-resonant waves, $\Omega_w(k_B, \pi)$, $\Omega_U(k_B, 0)$, and $\Omega_w(k_B, 0)$, respectively, and plotted against the flow Froude number, for each flow condition. The amplitude at the frequency of the upstream-propagating waves, $\Omega_w(k_B, \pi)$ has been measured only at flow conditions 5, 7, 10, 11, and 13, where $\Omega_w(k_B, \pi)$ was larger than 0.25 $\Omega_U(k_B, 0)$, and the effects of the upstream-propagating capillary waves were clearly distinguishable from the main spectral peak centred at zero frequency, in Figs. 8(b) and 8(c). The amplitude at the frequency of the downstream-propagating waves, $\Omega_w(k_B, 0)$, instead, was measured at all conditions where these waves could be observed, i.e., at all conditions shown in Figs. 8(b) and 8(c). For each type of wave, corresponding to a specific frequency, the amplitude of the Doppler spectra shown in Fig. 9 appears to increase exponentially with the Froude number. The lines shown in this figure were obtained by a least-squares fitting of the logarithm of the amplitudes of the Doppler spectra. The results suggest that the amplitude at the frequency of the non-dispersive Bragg-resonant waves, $\Omega_U(k_B, 0)$ increased proportionally to $\exp(10.7F)$ when the Froude number F varied between 0.30 and 0.68. The amplitude of the Doppler spectra at the frequency of the Bragg-resonant upstream-propagating capillary waves, $\Omega_w(k_B, \pi)$, was up to 100 times larger at the conditions where
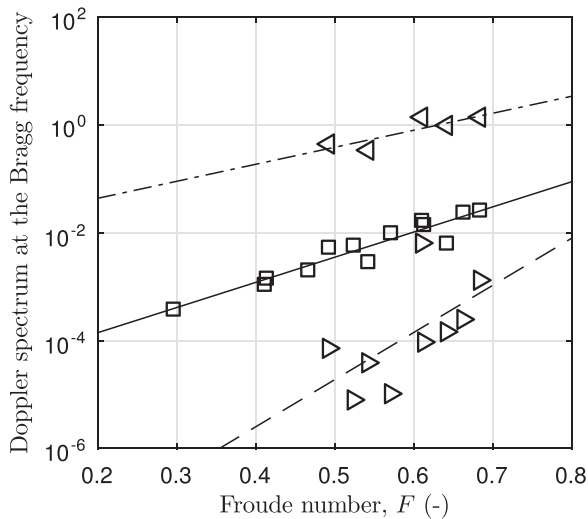
these waves could be identified clearly, and it increased like $\exp(7.3F)$ when the Froude number varied between 0.49 and 0.68. In the same range of Froude numbers, the amplitude of the Doppler spectra at the frequency of the downstream-propagating Bragg-resonant waves increased faster and proportionally to $\exp(20.1F)$. At these frequencies, the amplitude also varied more largely from the proposed exponential laws, which was explained by the rapid gradient of the measured spectra at the higher frequencies. This fact explains why at flow condition 10, which had the Froude number of 0.61, the Doppler spectrum at the frequencies of the non-dispersive waves and of downstream-propagating waves have a similar amplitude. In the remaining flow conditions, the ratio between these amplitudes varied between approximately 1000 (flow condition 8, $F = 0.57$) and 20 (flow condition 13, $F = 0.68$).

V. REMOTE MEASUREMENT OF THE SURFACE FLOW VELOCITY

The results presented in this study have important consequences for the ability to measure the mean surface velocity of turbulent flows remotely, based on the measurements of the Doppler spectra of airborne ultrasound. The experimental results suggest a large variability of the shape of these spectra at different Froude numbers. This can limit the reliability of airborne Doppler measurements of the surface velocity. The comparison with the numerical simulations based on a linear model of the surface suggests the importance of nonlinear modulations of the waves on the surface, or the presence of a broad spectrum of the small capillary waves which govern the backscattering of ultrasound. The inclusion of these phenomena in the simulations would allow a better parametrization of the measured spectra, and would improve the accuracy of the velocity measurements. Unfortunately, there are no known nonlinear models of practical use that apply to capillary waves propagating over turbulent flows, and the measurement of the angular spectrum of small capillary waves is difficult.

Having observed the dependence of the measured Doppler spectra on the flow Froude number, a set of simple methods that enable the estimate of the mean surface velocity within different limited ranges of Froude numbers is suggested. The first method corresponds to the one described in Ref. 6, and is based on the measurement of the two frequencies of the upstream- and downstream Bragg-resonant capillary waves, $\Omega_w(k_B, \pi)$ and $\Omega_w(k_B, 0)$, respectively. The mean surface velocity can then be determined as $U_0 = (\Omega_w(k_B, \pi) + \Omega_w(k_B, 0))/2k_B$. In order to apply this method, the two peaks at the frequencies $\Omega_w(k_B, \pi)$ and $\Omega_w(k_B, 0)$ need to be identified from corresponding peaks of the Doppler spectra. In Fig. 8, it was shown that these peaks may not be visible at low Froude numbers (lower than 0.49 in this study). At larger Froude numbers, only the peak of the upstream-propagating waves could be identified clearly from the measurements, and only at the conditions where $\Omega_w(k_B, \pi)$ was larger than $0.25\Omega_U(k_B, 0)$, in this study. This corresponds to the requirement that the mean surface velocity U_0 is larger than 133% of the phase velocity of the

FIG. 9. Amplitude of the measured Doppler spectra, evaluated at the frequency of the Bragg-resonant (◁) upstream-propagating capillary waves, $\Omega_w(k_B, \pi)$, (▷) downstream-propagating capillary waves, $\Omega_w(k_B, 0)$, and (□) non-dispersive waves propagating at the same velocity of the flow, $\Omega_U(k_B, 0)$. The lines have been found by a least-squares fitting of the logarithms of the amplitudes. (solid) $\propto \exp(10.7F)$, (dashed-dotted) $\propto \exp(7.3F)$, and (dashed) $\propto \exp(20.1F)$.

Bragg-resonant capillary waves in still water. The peak at the higher frequency of $\Omega_w(k_B,0)$ was difficult to identify in Figs. 8(b) and 8(c), because of the presence of the other peak at the frequency of non-dispersive waves, $\Omega_U(k_B,0)$, and because of the large width of the spectral peaks. Extrapolating the exponential fitting of the spectrum amplitudes at the frequencies of $\Omega_U(k_B,0)$ and $\Omega_w(k_B,0)$ to higher Froude numbers, it is expected that the effects of the downstream-propagating waves would become more easily recognizable at higher Froude numbers. The difficult identification of the high-frequency peak at intermediate Froude numbers can cause an ambiguity of the velocity estimations,[6] while the absence of both peaks at low Froude numbers makes the estimation of the flow velocity with the method employed in Ref. 6 infeasible.

The experimental results shown in Fig. 8 suggest different alternative approaches for the measurement of the flow velocity. At relatively low Froude numbers, the spectra shown in Fig. 8 have a relative maximum near the frequency of $\Omega_U(k_B,0)$, which can be easily identified. At these conditions, the mean surface velocity can be estimated simply based on the dispersion relation of non-dispersive waves, Eq. (5), as

$$U_0 = \Omega_U(k_B,0)/k_B, \tag{25}$$

where k_B is determined by the measurement setup, according to Eq. (1). The relative error of the flow mean surface velocities estimated with this method at the low Froude number conditions 1 to 4 based on the measured Doppler spectra presented in Fig. 8(a) was found to be smaller than 14%, and is shown in Fig. 10. Applying a similar approach to the dispersion relation of gravity-capillary waves, Eq. (5), one could obtain an alternative estimate of the velocity U_0 based on the measurement of the frequency of the upstream-propagating Bragg-resonant waves, $\Omega_w(k_B,\pi)$, as
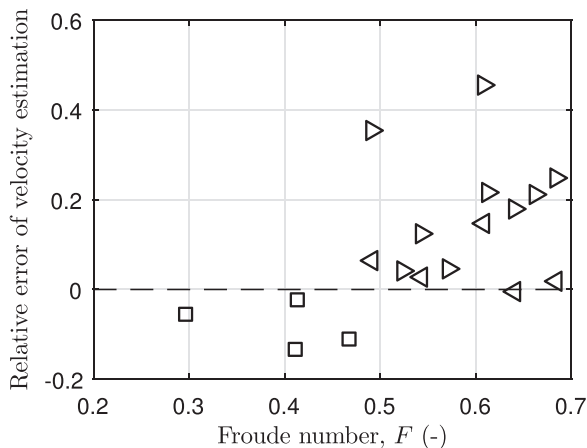
$$U_0 = \Omega_w(k_B,\pi)/k_B + c_0(k_B), \tag{26}$$

FIG. 10. Relative error of the estimations of the flow mean surface velocity based on the measurements of the Doppler spectra. ($\square$) Estimation based on the spectral peak at the frequency of non-dispersive waves, Eq. (25). ($\triangleleft$) Estimation based on the spectral peak at the frequency of the upstream-propagating capillary waves, Eq. (26). ($\triangleright$) Estimation based on the frequency of the downstream-propagating capillary waves (28), approximated by the frequency where the Doppler spectra become smaller than 5×10^{-6}.

where $c_0(k_B)$ is the phase velocity of gravity-capillary waves with wavenumber k_B in still water. For short Bragg-resonant waves and relatively large flow depths, $k_B H \gg 1$, $c_0(k_B)$ can be approximated as

$$c_0(k_B) = \sqrt{\left(\frac{g}{k_B} + \frac{\gamma}{\rho} k_B\right)}. \tag{27}$$

The frequency $\Omega_w(k_B,\pi)$ can be measured from a maximum of the measured Doppler spectra of Figs. 8(b) and 8(c), in those conditions where $U_0 > c_0(k_B)/0.75$. The relative error of the flow mean surface velocity estimations based on Eq. (26) applied to these conditions was found to be smaller than 15%, and is also shown in Fig. 10 as a function of the Froude numbers.

The two proposed alternative methods to estimate the flow mean surface velocity apply, respectively, to flows with low Froude numbers, or to flows with an intermediate or higher Froude numbers, where the flow mean surface velocity is relatively large. In the remaining flow conditions, the two frequencies $\Omega_w(k_B,\pi)$ and $\Omega_U(k_B,0)$ are difficult to identify. The frequency $\Omega_w(k_B,0)$ is equally difficult to measure due to the wide spectral peaks and to the presence of the peak at the frequency of non-dispersive waves. It is seen in Figs. 8(b) and 8(c), that the measured Doppler spectra decay rapidly at frequencies slightly higher than $\Omega_w(k_B,0)$. It is suggested to identify the cut-off frequency at which the spectra decay below an arbitrary threshold, and to use this frequency to approximate $\Omega_w(k_B,0)$. The mean surface velocity can then be estimated as

$$U_0 = \Omega_w(k_B,0)/k_B - c_0(k_B). \tag{28}$$

This method is expected to overestimate the actual mean surface velocity by an amount that depends on the widening of the Doppler spectra, and on the choice of the amplitude threshold. For this study, a threshold of 5 times the noise level was chosen, as it was smaller than the amplitude of the spectra at the frequency of $\Omega_w(k_B,0)$, across all conditions. The relative uncertainty of the flow mean surface velocity estimates obtained with this procedure was found to vary between 4% at flow conditions 6 and 8 and 35% and 46% at flow conditions 5 and 10, respectively, which had a higher mean flow depth. Being able to quantify the width of the Doppler peaks through inclusion of the nonlinear interactions may enable reducing these uncertainties. In all cases presented here, the value of the flow Froude number should be known in advance in order to be able to apply the correct measurement approach among the ones proposed. It is suggested that this could be achieved through iterative methods.

VI. CONCLUSIONS

The measurements of the Doppler spectra of airborne ultrasound backscattered by the rough dynamic surface of a range of shallow turbulent flows, and their numerical simulation based on the Kirchhoff approximation and on a linear random-phase model of the water surface, have been presented. Although the wide directivity of the acoustic

J. Acoust. Soc. Am. **142** (6), December 2017

Dolcetti *et al.* 3399

transducer in air did not allow for the measurements to be performed purely in the Fraunhofer zone, the results suggest that Bragg scattering associated with the direction of the maximum directivity was still the fundamental scattering mechanism for the experiments reported here. This mechanism produces peaks of the Doppler spectrum which are identifiable across different flow conditions. This finding supports previous observations based on microwave or radar sensors.[6] As a result, airborne ultrasound are proven to be a valid alternative for the remote measurement of the flow mean surface velocity in turbulent shallow flows.

The experimental and numerical results have provided a better insight about the behavior of the free surface of shallow turbulent flows, for the capillary waves with the wavelength of a few millimeters. Although the amplitude of these waves is believed to be only of a few micrometers, these short waves can have a considerable impact on the transfer of heat and gas across the water surface[35] and they are difficult to measure with alternative experimental techniques. A strong dependence of the Doppler spectra on the hydraulic flow conditions requires a good understanding of the behavior of the surface waves to make accurate interpretation of the surface velocity measurements obtained with Doppler remote measurement methods. The discrepancy between the predictions of the Doppler spectra obtained based on a simple linear surface model and their measurements in controlled laboratory conditions has evidenced the need for more accurate models of the free surface of turbulent flows, that include nonlinear interactions among waves on the surface, or a better characterization of their angular spectrum. These models would allow a better interpretation of the measurements, including the correct prediction of the width of the Bragg peaks of the acoustic Doppler spectra, and could improve the accuracy of the flow velocity estimations based on backscattering Doppler.

The analysis presented here enabled the quantification of the parameters that govern the shape of the Doppler spectra, and its relation with the flow conditions. The amplitude of the acoustic Doppler spectra at the frequencies that correspond to the frequencies of the Bragg-resonant surface waves was found to increase almost exponentially with the Froude number of the flow. Different rates of increase were observed for different types of surface waves, so that the shape of the measured spectra changed noticeably with the conditions of the flow. Empirical relations which link the shape of the Doppler spectra with the flow Froude number have been suggested. In previous studies, the apparently inconsistent behavior of the Doppler spectra was believed to be the main obstacle for the accurate remote estimation of the flow velocity of turbulent flows.[6] In this work, it was suggested to apply different approaches to the measurement of the mean surface velocity, depending on the range of flow conditions, to overcome this issue. If confirmed outside of the laboratory conditions, the results in this study would allow the different behaviors of the acoustic Doppler spectra to be accounted for, and could help the design of more accurate flow velocity remote measurement techniques based on Doppler.

[1]B. E. Parkins, "Scattering from the time-varying surface of the ocean," J. Acoust. Soc. Am. **42**, 1262–1267 (1967).

[2]R. H. Stewart and J. W. Joy, "HF radio measurements of surface currents," Deep-Sea Res. Oceanogr. Abstr. **21**, 1039–1049 (1974).

[3]W. J. Plant and W. C. Keller, "Evidence of Bragg scattering in microwave Doppler spectra of sea return," J. Geophys. Res.-Oceans **95**, 16299–16310, https://doi.org/10.1029/JC095iC09p16299 (1990).

[4]J. A. McGregor, E. M. Poulter, and M. J. Smith, "Ocean surface currents obtained from microwave sea-echo Doppler spectra," J. Geophys. Res.-Oceans **102**, 25227–25236, https://doi.org/10.1029/97JC00981 (1997).

[5]D. Barrick, "First-order theory and analysis of MF/HF/VHF scatter from the sea," IEEE Trans. Ant. Propag. **20**, 2–10 (1972).

[6]W. J. Plant, W. C. Keller, and K. Hayes, "Measurement of river surface currents with coherent microwave systems," IEEE T. Geosci. Remote **43**, 1242–1257 (2005).

[7]J. E. Costa, R. T. Cheng, F. P. Haeni, N. Melcher, K. R. Spicer, E. Hayes, W. J. Plant, K. Hayes, C. Teague, and D. Barrick, "Use of radars to monitor stream discharge by noncontact methods," Water Resour. Res. **42**, W07422, https://doi.org/10.1029/2005WR004430 (2006).

[8]M. Welber, J. Le Coz, J. B. Laronne, G. Zolezzi, D. Zamler, G. Dramais, A. Hauet, and M. Salvaro, "Field assessment of noncontact stream gauging using portable surface velocity radars (SVR)," Water Resour. Res. **52**, WR017906, https://doi.org/10.1002/2015WR017906 (2016).

[9]W. J. Plant, P. H. Dahl, and W. C. Keller, "Microwave and acoustic scattering from parasitic capillary waves," J. Geophys. Res.-Oceans **104**, 25853–25866, https://doi.org/10.1029/1999JC900168 (1999).

[10]K. Fukami, T. Yamaguchi, H. Imamura, and Y. Tashiro, "Current status of river discharge observation using non-contact current meter for operational use in Japan," in *Proceedings of the World Environmental and Water Resources Congress 2008: Ahupua'A*, Honolulu, HI (May 12–16, 2008), pp. 1–10.

[11]G. Dolcetti, K. V. Horoshenkov, A. Krynkin, and S. J. Tait, "Frequency-wavenumber spectrum of the free surface of shallow turbulent flows over a rough boundary," Phys. Fluids **28**, 105105 (2016).

[12]J. C. Burns, "Long waves in running water," Math. Proc. Cambridge **49**, 695–706 (1953).

[13]J. D. Fenton, "Some results for surface gravity waves on shear flows," IMA J. Appl. Math. **12**, 1–20 (1973).

[14]F. G. Bass and I. M. Fuks, "Wave scattering from statistically rough surfaces," Vol. 93 of *International Series in Natural Philosophy* (Oxford Pergamon Press, Oxford, 1979), p. 225.

[15]P. M. Morse and K. U. Ingard, *Theoretical Acoustics* (Princeton University Press, Princeton, 1968), p. 381.

[16]J. V. Toporkov and G. S. Brown, "Numerical simulations of scattering from time-varying, randomly rough surfaces," IEEE Trans. Geosci. Remote **38**, 1616–1625 (2000).

[17]K. V. Horoshenkov, A. Nichols, S. J. Tait, and G. A. Maximov, "The pattern of surface waves in a shallow free surface flow," J. Geophys. Res.-Earth **118**, 1864–1876, https://doi.org/10.1002/jgrf.20117 (2013).

[18]G. Dolcetti, "Remote monitoring of shallow turbulent flows based on the Doppler spectra of airborne ultrasound," Ph.D. dissertation, The University of Sheffield, Sheffield, 2017, Chap. 5.

[19]M. S. Longuet-Higgins, "The statistical analysis of a random, moving surface," Philos. Trans. R. Soc. A **249**, 321–387 (1957).

[20]T. Elfouhaily, B. Chapron, K. Katsaros, and D. Vandemark, "A unified directional spectrum for long and short wind-driven waves," J. Geophys. Res.-Oceans **102**, 15781–15796, https://doi.org/10.1029/97JC00467 (1997).

[21]S. A. Kitaigordskii, V. P. Krasitskii, and M. M. Zaslavskii, "On Phillips' theory of equilibrium range in the spectra of wind-generated gravity waves," J. Phys. Oceanogr. **5**, 410–420 (1975).

[22]R. Savelsberg and W. Van De Water, "Experiments on free-surface turbulence," J. Fluid Mech. **619**, 95–125 (2009).

3400   J. Acoust. Soc. Am. **142** (6), December 2017

Dolcetti *et al.*

[23]S. Nazarenko and S. Lukaschuk, "Wave turbulence on water surface," Annu. Rev. Condens. Matter Phys. **7**, 61–88 (2016).

[24]H. E. Krogstad, "The directional wave spectrum," in *Cost Action 714, Measuring and Analysing the Directional Spectra of Ocean Waves*, edited by D. Hauser, K. K. Kahma, H. E. Krogstad, S. Lehner, J. Monbaliu, and L. R. Wyatt (Office for Official Publications of the European Communities, Luxembourg, 2005), p. 45.

[25]E. I. Thorsos, "The validity of the Kirchhoff approximation for rough surface scattering using a Gaussian roughness spectrum," J. Acoust. Soc. Am. **83**, 78–92 (1988).

[26]S. N. Chandler-Wilde, "The boundary element method in outdoor noise propagation," Proc. Inst. Acoust. **19**, 27–50 (1997).

[27]A. Krynkin, K. V. Horoshenkov, A. Nichols, and S. J. Tait, "A non-invasive acoustical method to measure the mean roughness height of the free surface of a turbulent shallow water flow," Rev. Sci. Instrum. **85**, 114902 (2014).

[28]W. C. Keller, W. J. Plant, R. A. Petitt, and E. A. Terray, "Microwave backscatter from the sea: Modulation of received power and Doppler bandwidth by long waves," J. Geophys. Res.-Oceans **99**, 9751–9766, https://doi.org/10.1029/94JC00082 (1994).

[29]J. C. Preisig and G. B. Deane, "Surface wave focusing and acoustic communications in the surf zone," J. Acoust. Soc. Am. **116**, 2067–2080 (2004).

[30]J. T. Johnson, J. V. Toporkov, and G. S. Brown, "A numerical study of backscattering from time-evolving sea surfaces: Comparison of hydrodynamic models," IEEE Trans. Geosci. Remote **39**, 2411–2420 (2001).

[31]J. W. Wright, "A new model for sea clutter," IEEE Trans. Ant. Propag. **16**, 217–223 (1968).

[32]G. R. Valenzuela, "Scattering of electromagnetic waves from a tilted slightly rough surface," Radio Sci. **3**, 1057–1066, https://doi.org/10.1002/rds19683111057 (1968).

[33]W. C. Keller and J. W. Wright, "Microwave scattering and the straining of wind-generated waves," Radio Sci. **10**, 139–147, https://doi.org/10.1029/RS010i002p00139 (1975).

[34]C. L. Rino, T. L. Crystal, A. K. Koide, H. D. Ngo, and H. Guthart, "Numerical simulation of backscatter from linear and nonlinear ocean surface realizations," Radio Sci. **26**, 51–71, https://doi.org/10.1029/90RS01687 (1991).

[35]D. Lakehal, M. Fulgosi, G. Yadigaroglu, and S. Banerjee, "Direct numerical simulation of turbulent heat transfer across a mobile, sheared gas-liquid interface," J. Heat Trans. **125**, 1129–1139 (2003).

[36]G. Dolcetti and A. Krynkin, "Doppler spectra of airborne ultrasound forward scattered by the rough surface of open channel turbulent water flows," J. Acoust. Soc. Am. **142**(5), 3122–3134 (2017).